OPTICA

# Suspended nanophotonic waveguide for isotope-specific $CO_2$ detection

Jehona Salaj,[1] Marek Vlk,[1] Roman Zakoldaev,[1] Ragnar Seton,[1] Jiří Čtyroký,[2] Sebastián Alberti,[1] Astrid Aksnes,[3] and Jana Jágerská[1,*]

[1]Department of Physics and Technology, UiT The Arctic University of Norway, Klokkargårdsbakken 35, NO-9037, Tromsø, Norway
[2]Department of Fiber Lasers and Nonlinear Optics, CAS Institute of Photonics and Electronics, Chaberská 57, 18200 Prague, Czech Republic
[3]Department of Electronic Systems, Norwegian University of Science and Technology, O.S. Bragstads plass 2b, NO-7491, Trondheim, Norway
*jana.jagerska@uit.no

Received 25 June 2024; revised 14 October 2024; accepted 29 October 2024; published 11 December 2024

**The spectroscopic detection of gases and their stable isotopes holds significant value in bio-sciences and climate studies. However, achieving high precision has long been confined to bulky and costly equipment. In this work, we introduce a nanophotonic waveguide that is capable of detecting $CO_2$ gas down to 20 parts per billion, and for the first time perform accurate stable isotope ratio measurements. The waveguide leverages a suspended membrane design with microstructured cladding, providing a high evanescent field confinement factor of 102%, moderate loss of 3.4 dB/cm, and effective suppression of etalons. The $\delta^{13}C$ isotope ratio precision of 0.2‰ was achieved, replicating the performance of high-end laser absorption spectrometers. This marks the inaugural instance of on-chip, isotope-specific gas detection with a compact and cost-efficient system scalable to sensor networks.** 

https://doi.org/10.1364/OPTICA.533710

## 1. INTRODUCTION

Laser absorption spectroscopy (LAS) is a widely used technique for identifying molecules and their concentrations in gaseous samples. When molecules interact with mid-infrared (MIR) radiation, covering wavelengths from 2 to 20 μm, they manifest absorption lines at the frequencies corresponding to their vibrational and rotational motion [1]. These are known as molecular fingerprints. MIR LAS systems probe these fingerprints to sensitively and selectively detect and quantify trace amounts of greenhouse gases, pollutants, and toxic gaseous substances [2]. Among them, carbon dioxide ($CO_2$) has the highest impact on climate change through radiative forcing [3], and its global concentration continues to increase every year. Monitoring variations in atmospheric $CO_2$ and its stable isotopes is crucial for understanding human impacts on the natural carbon cycles [4] and for refining climate models [5]. Furthermore, the isotope ratio ($\delta^{13}C$) is invaluable in biological research, providing insights into metabolic processes [6], nutrient allocation [7], as well as in the fields of archaeology [8] and paleontology [9] to gather dietary and environmental information about ancient species for instance.

High-end LAS systems based on multipass cells or stabilized high-finesse optical cavities have pushed the limit of detection (LoD) down to impressive parts-per-trillion (ppt) [10–13] or even parts-per-quadrillion (ppq) [14,15]. In parallel, research efforts have been aimed at miniaturizing these systems, driven by the increasing demand for sensors that are both portable and scalable. While there has been a significant progress in compact MIR laser sources and detectors, such as interband and quantum cascade lasers, and superlattice detectors, the overall size reduction of LAS systems is still limited by the gas cell. Conventional gas cells and cavities based on free-space optics accumulate effective optical pathlengths ranging from several meters [16] to kilometers [17], but are bulky and costly. Moreover, they require sophisticated alignment, extensive stabilization, and large sample volumes, which decreases gas exchange rates and the system response.

Advancing full on-chip integration involves substituting the gas cell with an integrated counterpart, such as a waveguide chip. However, the performance of MIR waveguides has been plagued by significant propagation losses, spurious etalon effects, and poor interaction with the sample. One promising direction in waveguide sensor design focuses on enhancing the external evanescent field confinement factor, $\Gamma_e$. The confinement factor quantifies the light–matter interaction in waveguides, as theoretically elaborated by Veldhuis *et al.* [18]. We have recently demonstrated a suspended membrane rib waveguide operating in TM polarization that produces extensively delocalized field with $\Gamma_e = 107\%$ [19], which implies a stronger mode–analyte interaction than with a free-space beam. The waveguide geometry has simultaneously minimized interaction with the waveguide material, which has reduced facet and defect reflections and produced clear spectral signal in transmission free of spurious etalons. With this design, we have achieved 7 ppm LoD with acetylene at 2566 nm, the first ppm-level gas detection with an on-chip LAS device. Yet, the rib waveguide design has proved challenging due to intrinsic loss through TM–TE mode conversion [20], which, together with

the material absorption loss, constrained the physical waveguide length to at most a few centimeters.

An alternative design of high $\Gamma_e$ waveguides incorporates subwavelength gratings. Kita *et al*. [21] have provided a theoretical analysis of benefits of subwavelength grating waveguides over conventional strip waveguides in the context of sensing. Liu *et al*. [22] have later experimentally demonstrated a subwavelength comb waveguide facilitating acetone detection with an excellent 2.5 ppm LoD at 7 μm wavelength. Its intricate subwavelength design, however, does not readily accommodate operation at shorter wavelengths due to the minimal features becoming excessively small and impractical for fabrication.

In this paper, we combine our earlier approach and that of Kita *et al*. [21], leveraging the large field confinement of a thin-film membrane while using a two-dimensional subwavelength array to confine the mode laterally. We demonstrate that this novel design simultaneously provides strong light–matter interaction and enables intrinsically lossless guiding. We further showcase a waveguide-based detection of the two most abundant $CO_2$ isotopes at 4.345 μm down to ppb levels. The increased sensitivity enables the first instance of on-chip isotope-specific gas detection with a precision comparable to open-path high-end systems.

## 2. WAVEGUIDE DESIGN

Figure 1(a) outlines the waveguide design based on a free-standing silicon nitride (SiN) membrane suspended above a silicon substrate. Low-stress SiN on silicon was selected as the waveguide material because of its commercial availability and robust fabrication support. Its broad transparency window spanning from 0.28 to 5 μm [23] fits with the objective of spectroscopic $CO_2$ detection around 4.3 μm. Mechanical properties of low-stress SiN are favorable for the production of high-aspect-ratio membranes and MEMS (micro-electro-mechanical systems) [24].

Our waveguide features a triangular lattice of holes as lateral cladding with the waveguide core defined by a line defect in the lattice. While such geometry is common in photonic crystal waveguides, this particular layout utilizes subwavelength dimensions for the lattice, which ensures lateral mode confinement via index guiding rather than through a band-gap effect.

Importantly, the TM mode of this waveguide, favored for sensing due to its larger evanescent field confinement, is completely free of radiation loss caused by coupling with TE planar modes, which typically takes place in rib waveguides [19,20]. Owing to the symmetry of the waveguide cross-section in both orthogonal directions, the symmetry of all field components of the TM mode is just opposite to that of the components of the TE planar modes, which prevents their mutual coupling. As detailed in Supplement 1 S1,

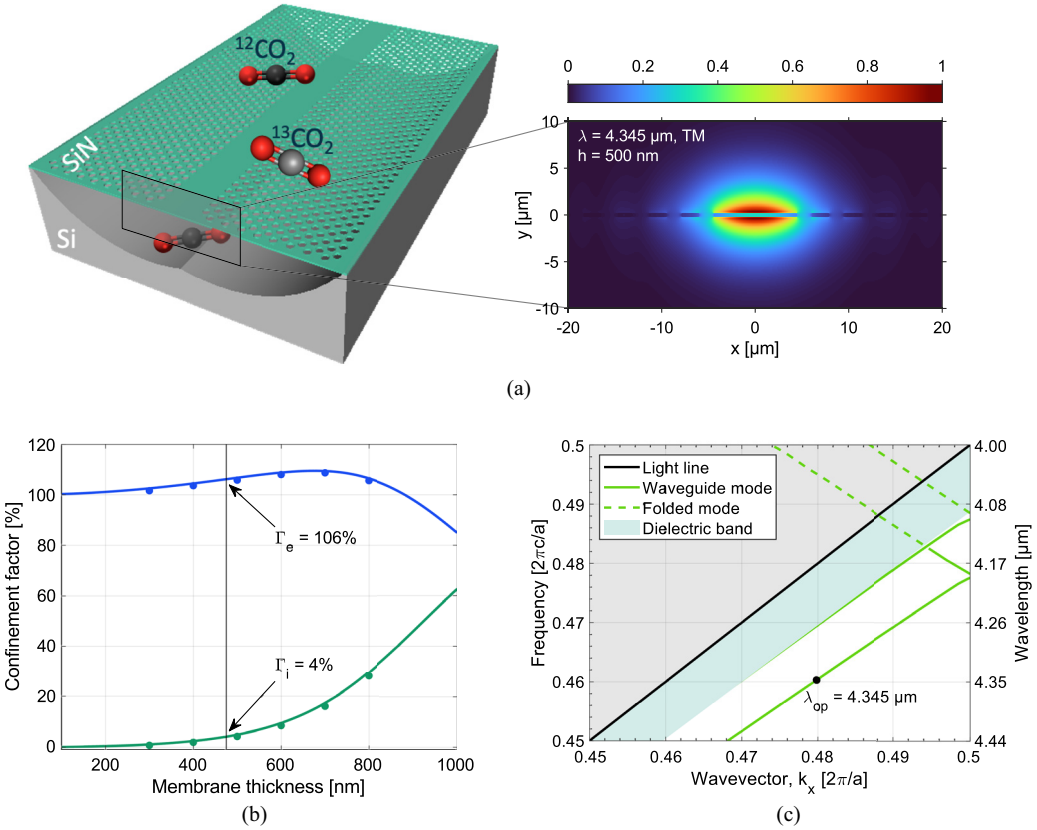


**Fig. 1.** Waveguide design. (a) Three-dimensional schematic representation of the waveguide highlighting the $|\boldsymbol{E}|$ field distribution of the TM mode at the waveguide cross-section; (b) simulated internal and external confinement factors at 4.3 μm as a function of SiN membrane thickness. 2D simulation performed using Lumerical FDE for a simple unpatterned membrane (lines) is compared to full 3D Lumerical FDTD simulation of the waveguide with microscrutured cladding (dots). The thickness of the fabricated device is indicated by a vertical line (black), and the corresponding confinement factors are displayed; (c) the band diagram of the waveguide characterized by a lattice period a = 2 μm, hole radius r = 0.8 μm, and membrane thickness h = 0.5 μm. The dark green shaded region represents the photonic crystal dielectric band, the black line denotes the lightline, and the green lines indicate the index-guided waveguide modes. The black circle marks the operating point at a wavelength of 4.345 μm.

the TM mode can thus be considered a pure symmetry protected bound mode in the continuum (BIC) and is inherently lossless.

The structural dimensions of the waveguide were optimized to provide the best sensing performance, i.e., the lowest LoD for the target $CO_2$ molecules. The most critical design parameter is the membrane thickness $h$, which largely determines the vertical field confinement. This confinement, in turn, governs the mode interaction with both the surrounding environment and the membrane material itself. We respectively quantify these interactions through the external ($\Gamma_e$) and internal ($\Gamma_i$) confinement factors, which are expressed analytically as follows [25]:

$$\Gamma_{e,i} = \frac{n_g}{n_{e,i}} \frac{\int_Z \iint_{e,i} \varepsilon |\boldsymbol{E}|^2 \mathrm{d}x\mathrm{d}y\mathrm{d}z}{\int_Z \iint_{-\infty}^{\infty} \varepsilon |\boldsymbol{E}|^2 \mathrm{d}x\mathrm{d}y\mathrm{d}z}, \quad (1)$$

where $n_g$ is the mode group index, $n_{e,i}$ is the refractive index of the air cladding (external, $e$) and the waveguide core (internal, $i$), respectively. $\varepsilon$ is the permittivity, $\boldsymbol{E}$ the electric field, and the integration in the $z$-direction runs over one structure period $Z$. The expression for the confinement factor has been initially derived for waveguides with translational symmetry, but the generalized form in Eq. (1) also applies to periodic structures [22].

It is crucial to recognize that the confinement factors are not solely determined by the modal power fractions in the cladding or the core. Instead, they are influenced by both the modal fraction and the waveguide dispersion, captured through the group index $n_g$. This means that the slower propagation of light in waveguides compared to free space additionally enhances light–matter interactions. The synergistic effect of field delocalization and dispersion can lead to $\Gamma$ exceeding unity, resulting in stronger absorption in the cladding or core material than what is achieved with a free-space beam.

In Fig. 1(b) we simulated the confinement factor values of the fundamental TM mode versus the SiN membrane thickness, assuming the SiN refractive index $n_i = 2.1$. The external confinement factor $\Gamma_e$ shows a broad maximum exceeding 100% centered at 700 nm thickness, while $\Gamma_i$ monotonously increases with the thickness $h$.

Absorption by the analyte molecules is directly scaled by $\Gamma_e$ following the generalized Lambert-Beer law $I = I_0 \exp(-\alpha \Gamma_e L)$, which implies that increasing $\Gamma_e$ proportionally increases the absorption signal. Maintaining a low $\Gamma_i$, however, is equally important for optimal sensor performance, although this has been previously little addressed in literature. $\Gamma_i$ determines the propagation loss of the waveguide mode due to interaction with the material of the waveguide core. This includes material absorption loss as well as losses due to volumetric scattering at defects, sidewall roughness, and other material and structural imperfections. Low $\Gamma_i$ thus facilitates long, low-loss waveguides, thereby also enhancing the overall absorption signal. As detailed in Supplement 1 S2, in waveguides exhibiting material absorption larger than a fraction of dB/cm, minimizing the $\Gamma_i$ is essential; the lowest LoD is achieved for lowest $\Gamma_i$ and not at the maximum of the relatively flat $\Gamma_e$. In addition, low $\Gamma_i$ results in suppressed reflections contributing to mitigation of spurious etalons and better signal-to-noise ratio (SNR). Overall, optimal waveguide performance is achieved by utilizing the thinnest membrane that maintains mechanical stability while adequately confining the mode. In this work, a good balance is found with a commercially available membrane thickness $h = 0.5$ μm, which exhibits $\Gamma_e = 106\%$ and $\Gamma_i = 4\%$ at 4.3 μm wavelength.

The waveguide lateral dimensions and the periodicity of the cladding pattern were determined through a simulation of the full dispersion diagram using MIT Photonic-Bands. A waveguide core consisting of five missing rows of holes (W5) guarantees a single mode operation and proper lateral confinement, while the hole period, a = 2 μm, is still perceived by the mode as sub-wavelength. The hole radius, $r$, should be in the range of 0.8–0.9 μm to enable waveguide bends as tight as 1.5 mm while maintaining good mechanical stability. Figure 1(c) shows the dispersion of the waveguide mode (green line), also marking the operating point at the frequency $a/\lambda = 0.46$, corresponding to the wavelength of 4.345 μm. At this frequency, the mode is found well below the dielectric band of the photonic crystal cladding (dark green region), which implies its index-guided nature. Located below the lightline, the mode is confined in both orthogonal directions.

Complementary 3D Lumerical FDTD simulations of the waveguide give internal and external confinement factor values that closely match the values obtained for the un-patterned membrane as also shown in Fig. 1(b). Additional Lumerical simulations show that a lateral cladding width of approximately 30 μm corresponding to 17 rows of holes is sufficient to mitigate lateral leakage losses, as well as bending losses for radii up to 1.5 mm. This bend radius allows for a waveguide up to 20 cm long to be folded in an Archimedean spiral pattern on a chip with a footprint of just 1 $cm^2$. An air gap under the membrane larger than 15 μm is necessary in order to keep the theoretical loss associated with mode leakage into the substrate below 0.1 dB/cm.

## 3. FABRICATION

The waveguides were fabricated in commercially available 0.5 μm thick low-stress SiN films deposited through low-pressure chemical vapor deposition (LPCVD) on a silicon substrate (UniversityWafer Inc). The subwavelength cladding design allows for a convenient one-mask fabrication process as opposed to other approaches [26]. It entails defining the hole pattern using maskless UV photolithography in a Cr hard mask, followed by a two-step ICP RIE etching. The initial etching step utilizes $CF_4$ to transfer the cladding hole pattern into the SiN layer. The waveguide cladding holes simultaneously provide access to the underlying silicon material. The subsequent membrane release is facilitated through isotropic $SF_6$ etching of the underlying Si substrate. More details on fabrication are available in Supplement 1 S3.

Straight and S-shaped waveguides of lengths varying between 0.5 and 3.0 cm were fabricated and visually examined through SEM imaging. Figure 2(a) shows the structural characteristics of the lateral cladding, including irregularities in the hole lattice manifested through a Moiré pattern. This irregularity is a result of the resolution reaching the technological constraints of the maskless writing process and can be eliminated by using different patterning techniques such as photomask-based lithography or nanoimprint lithography. The inset also shows that the hole edges exhibit roughness and a slight variability in their dimensions and shapes. Nevertheless, the average hole radius of 0.8 μm was maintained, matching the design. The hole irregularity and roughness appear to have a minimal impact on the light guiding, causing no detectable scattering during operation. As further shown in the cross-sectional view of the fabricated waveguide in Fig. 2(b), the waveguide is suspended approx. 50 μm above the silicon substrate, leaving enough space for the extended TM mode and preventing

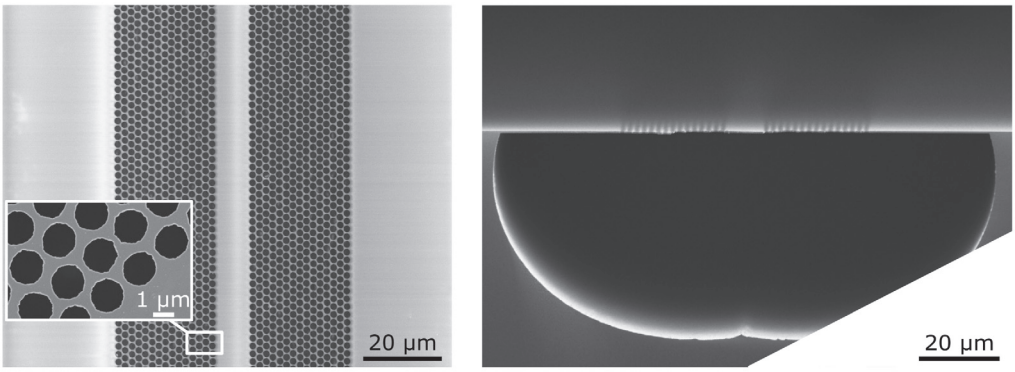


**Fig. 2.** SEM images of the fabricated waveguides: (a) top view of the waveguide, with inset giving a magnified view of the waveguide cladding; (b) cross-sectional view of the waveguide facet.

any leakage into the substrate. The membrane thickness was measured at $h \approx 475$ nm, i.e., 25 nm less than the nominal thickness, which is attributed to a partial etching of $Si_3N_4$ by the $SF_6$ plasma during the membrane release.

## 4. WAVEGUIDE SENSOR PERFORMANCE

### A. Experimental Setup

The waveguide performance for LAS was evaluated using an experimental setup schematically shown in Fig. 3. An interband cascade distributed feedback (DFB) laser (Nanoplus) electrically tuned between 4.3440 to 4.3465 µm was employed as the light source. This spectral range was chosen as it encompasses several absorption lines of $CO_2$ isotopes $^{12}CO_2$ and $^{13}CO_2$. In particular, the presence of two strong $^{12}CO_2$ and $^{13}CO_2$ lines with sufficient frequency separation and comparable amplitudes at their natural abundance is optimal for precise determination of the $\delta^{13}C$ isotope ratio. The laser beam was coupled into and out of the waveguide through the chip facets using a pair of aspheric lenses (NA = 0.56). The transmitted signal was registered by a mercury cadmium telluride photovoltaic detector (Vigo, PVI-4TE-5). Additionally, an MIR camera (Telops, FAST M350) provided a top-view image of the waveguide, aiding the coupling process and monitoring potential light scattering along the waveguide.

During spectroscopic measurements, the waveguide chip was fixed in a gas cell of closely matched dimensions in order to maintain controlled gas concentrations and pressure. $CO_2$ (Linde, $CO_2$ bioair, 5%) and $N_2$ (Linde, $\geq$ 99.999%) gases were mixed using flow controllers (Vögtlin, GSC-A9TA) to achieve concentrations ranging from 500 to 50000 ppm. The gas mixture was then continuously injected into the cell at a constant rate of 25 mL $min^{-1}$. We maintained the pressure in the cell with a pressure controller (Bronkhorst, El-press) connected to a vacuum pump (VWR, PM20405-86), stabilizing it at either 1 atm or 0.4 atm. Active temperature stabilization of the chip was not implemented, given that the minimal light interaction with the waveguide inherently leads to low sensitivity to temperature variations. To prevent $CO_2$ absorption outside the gas cell, the entire setup was enclosed and flushed with $N_2$.

### B. Propagation Loss

The waveguide propagation and coupling losses were measured at a fixed wavelength of 4.345 µm using the cutback method. Figure 4 shows the insertion loss as a function of the waveguide length measured on both straight and S-shaped waveguides, normalized to the transmission through the setup after the waveguide has been removed. A linear fit to the data provides the propagation loss of $3.4 \pm 0.3$ dB $cm^{-1}$. The loss of the S-shaped waveguide (bend radii of 1.6 mm) closely aligns with the losses measured in the straight waveguides, implying that the bending losses are

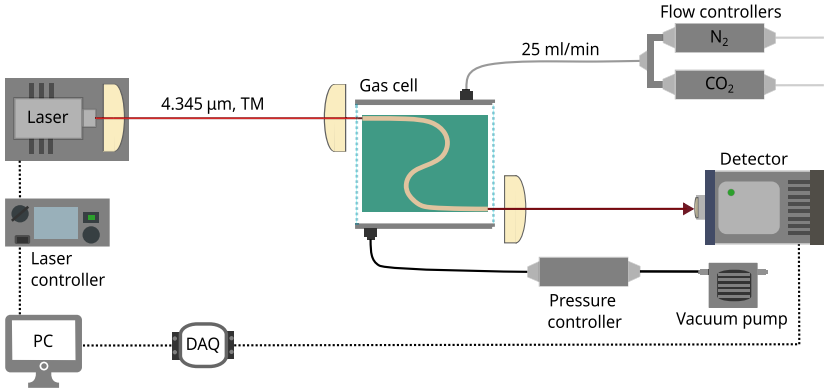


**Fig. 3.** Experimental setup for waveguide-based $CO_2$ gas spectroscopy, comprising the optical path, gas-flow system, and electronics for synchronous laser driving and data acquisition (DAQ).

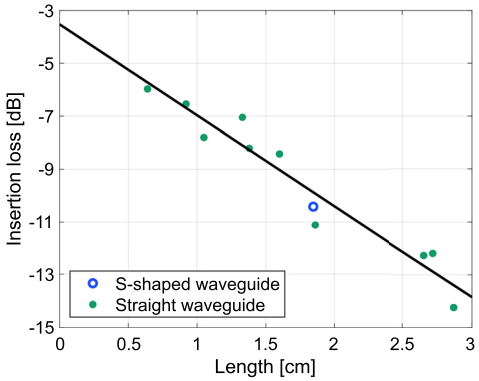


**Fig. 4.** Experimental insertion loss measured using the cut-back method on both straight and S-shaped waveguides. The slope gives a propagation loss of $3.4 \pm 0.3$ dB cm$^{-1}$, while the linear fit extrapolated for length = 0 indicates a coupling loss of $1.7 \pm 0.6$ dB per facet.

negligible. The intercept of the fit with the $y$-axis further provides an estimate of the coupling loss, which is equal to $1.7 \pm 0.6$ dB per facet.

As no scattering was observed from the surface except for a few point-defects, and the absorption loss by the ambient $CO_2$ is expected below 0.002 dB/cm, we hypothesize that a major portion of the measured loss is due to material absorption in SiN. Assuming internal confinement $\Gamma_i = 4\%$, the measured loss would imply a bulk absorption of 87.5 dB cm$^{-1}$. Although such loss seems high, the corresponding extinction ratio of $k = 0.0007$ is of the same order as and even lower than $k = 0.0017$ reported for non-stoichiometric SiN at 4.345 μm wavelength [23]. It is evident that SiN can realize low-loss waveguides in the MIR only if the $\Gamma_i$ is very low.

On the other hand, experimental coupling losses are among the lowest reported in end-fire coupling configurations without using any specialized couplers, which represents a marked advantage of using air-like waveguide modes. The coupling loss can be optimized even further by matching the waveguide mode to the free-space or laser output beam profile through fine adjustments to the membrane thickness and waveguide core width.

### C. Confinement Factor

All subsequent measurements were performed with an S-shaped waveguide of a total length of 20 mm patterned on a chip with a 1 cm × 1 cm footprint. This waveguide length has been identified as optimal in our experimental setup, expected to yield the lowest achievable LoD as detailed in Supplement 1 S4. Any further increase in the waveguide length would not enhance the detection limit, as the benefit of a longer path length would be cancelled out by a decrease in the signal-to-noise ratio.

Free-space LAS systems are generally regarded as calibration-free due to the direct fit of measured data to a calibrated database, resulting in absolute concentration values. However, even such systems often undergo one calibration step to compensate for, e.g., path length uncertainties and systematic errors in data processing. This calibration becomes essential for waveguide-based LAS systems, where there is an inherent uncertainty in the external confinement factor $\Gamma_e$, which alters the interaction strength in comparison to free space. The spectroscopy measurements involved two successive steps of sensor calibration and actual trace gas detection.

First, we performed the waveguide sensor calibration by measuring the reference gas $^{12}CO_2$ concentrations in 5000 ppm decrements ranging from 50000 to 5000 ppm and correlating the measurement results to a measurement in free space. The free-space measurement was conducted with the same gas mixing ratios, same setup, gas cell, and the same data processing routine, but with the waveguide and the coupling aspheric lenses removed.

For each concentration step, the calibration gas flow was first left to stabilize as shown in Fig. 5(a). The averaging durations for most steps are in the range of 200 s, and specifically in the inset, gray bands highlight the 192.4 s (281 points) averaging span. The duration of averaging was algorithmically determined to avoid including any part of the signal related to a change in concentration. For each data point, the laser frequency was swept across the target wavelength range at a rate of 216 Hz. An FPGA-based data acquisition module was employed to synchronously acquire and pre-average 128 spectra, which were then transferred to the computer for further processing. Obtained spectra were normalized by a baseline recorded in an $N_2$ atmosphere, then continuously fitted with calibrated spectra from the HITRAN2020 database [27].

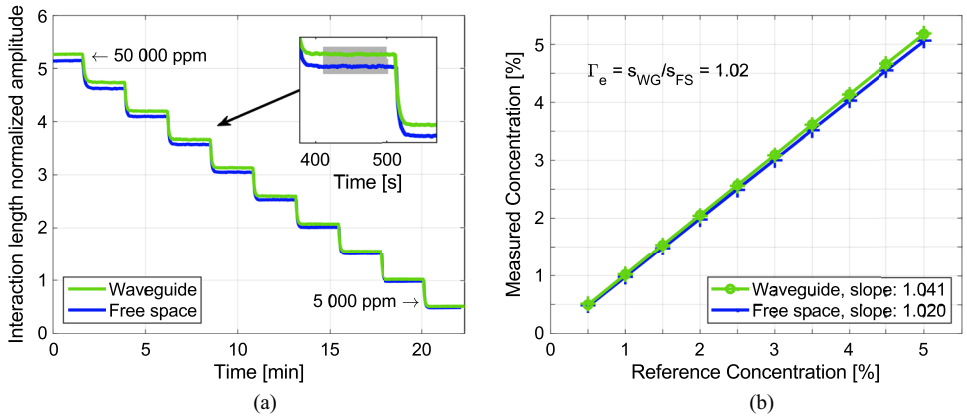


**Fig. 5.** Evaluation of linearity and calibration. (a) The system's response to a step-wise reduction in reference $^{12}CO_2$ concentrations from 50000 to 5000 ppm at a constant pressure of 0.4 atm. The gray box delineates the data subset used for plots in (b). (b) A calibration graph comparing the measured $^{12}CO_2$ concentration against its reference values for both the waveguide and the free-space configurations. The relative slope difference reflects the enhanced light-matter interaction in the waveguide, while the ratio of the slopes yields an experimental confinement factor of 102%.

More details about the data acquisition and processing are given in Supplement 1 S5.

Figure 5(b) presents the measurement results with calibration constants of 1.04 retrieved for the waveguide and 1.02 for the free space calibration. The near-unity slope observed in the free-space case is as expected, with a minor 2% deviation attributed to the error in the reference concentration (5% concentration uncertainty in the gas cylinder plus the uncertainty in flow rates), path length uncertainty, and error in the data processing step. The latter can result from, for example, inaccuracy in frequency scale calibration and subsequent deviation of the baseline or spectral fit. Measurements through the waveguide consistently indicated higher concentrations, confirming predictions about enhanced light–matter interaction in a waveguide with $\Gamma_e > 100\%$. Notably, linearity of measured concentrations across a dynamic range spanning one order of magnitude was maintained. The experimental confinement factor derived as a ratio of the respective slopes, $\Gamma_e = 102\%$, is slightly inferior but generally well-matched to the simulated value of 106%.

### D. $CO_2$ Detection

Following the calibration, we proceeded to measure the $CO_2$ gas mixture with a fixed concentration of 5000 ppm at pressures of 0.4 atm (Fig. 6). The reduced pressure of 0.4 atm was chosen to decrease the linewidth of the absorption lines that is in our experimental conditions determined by the collision (pressure) broadening (see Supplement 1 S5 for comparison of 1.0 and 0.4 atm spectra). This reduces the cross-talk between individual isotopes, enabling a more precise baseline definition and consequently improving the detection accuracy.

The experimental spectra reveal distinct absorption peaks for the $CO_2$ stable isotopes: $^{12}CO_2$ ($^{16}O^{12}C^{16}O$ or 626) and $^{13}CO_2$ ($^{16}O^{13}C^{16}O$ or 636). The spectrum also includes transition lines of the $^{16}O^{12}C^{18}O$ (628), which have to be accounted for in the fit to obtain a good match between the experimental data and the database spectra, but their absorption signal was not sufficient for precise concentration quantification. Remarkably, the experimental spectrum is smooth with no perceivable etalon fringes or interferometric noise, validating the success of etalon suppression with a waveguide of low $\Gamma_i$. The excellent overlap between the experimental data and the fit indicates that the linear absorption model implemented in HITRAN can be used, despite the fact that photonic waveguides due to their microscale field confinement achieve considerably higher optical intensities than a free-space beam.

To quantify the sensing performance of our waveguide, we evaluated the precision and LoD by analyzing time-series data of fixed concentration measured over an extended time interval of 450 s. Figure 7 plots a representative time series recorded simultaneously for both $^{12}CO_2$ and $^{13}CO_2$ isotopes at a concentration of 5000 ppm in $N_2$. Each set of time-series data is complemented by an Allan deviation plot, which is used to determine the optimal integration time for our waveguide spectroscopy system and to calculate the precision. At an integration time of 1 s, the $1-\sigma$ precision was established at 6 ppm for $^{12}CO_2$ and 65 ppb for $^{13}CO_2$. Upon extending the averaging period to 40 s, we achieved an improved precision of 2 ppm for $^{12}CO_2$ and 34 ppb for $^{13}CO_2$. The LoD was subsequently evaluated through an analogous procedure with pure $N_2$ flow. The $1-\sigma$ LoD was 1 ppm for $^{12}CO_2$ and 21 ppb for $^{13}CO_2$. The comparable values of LoDs and precisions at high concentrations are an independent confirmation that comparable precision can be obtained in the detection range of 0–5000 ppm, and that the gas presence leading to, e.g., refractive index changes, does not have a substantial effect on the sensor performance. This would not be the case in the presence of etalon fringes, which move with varying gas concentration, compromising the sensor stability and LoD.

### E. $\delta^{13}C$ Isotope Ratio Measurement

The isotope ratio $\delta^{13}C$ is defined as the relative difference in the isotopic composition of a sample compared to that of Vienna Pee Dee Belemnite (VPDB) standard reference [28]. The calculation employs the following equation:

$$\delta^{13}C = \left(\frac{R_{\text{sample}}}{R_{\text{standard}}} - 1\right) \times 1000, \tag{2}$$

where $R_{\text{sample}}$ is the ratio of the abundance of the heavy isotope $^{13}CO_2$ to the light isotope $^{12}CO_2$, and $R_{\text{standard}} = 0.0112372$ is the known ratio of these isotopes in the VPDB. We concentrated our experimental efforts on quantifying the accuracy and precision of the $\delta^{13}C$ measurement. The accuracy was evaluated from the isotope ratio measurement at varying $CO_2$ concentrations in

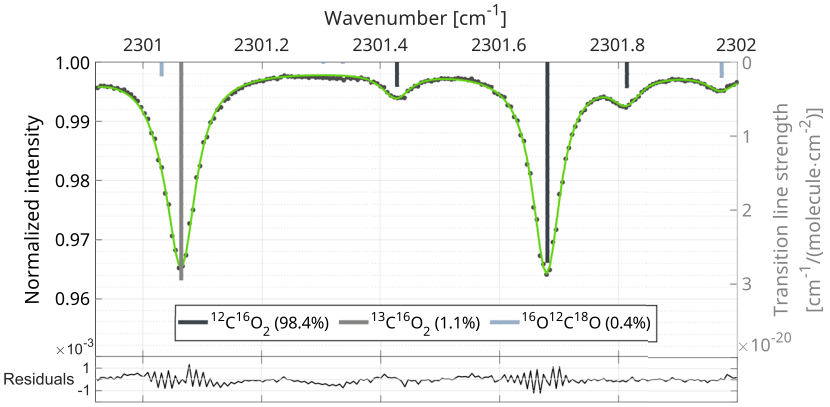


**Fig. 6.** Baseline-corrected 1.66 Hz experimental transmission spectrum obtained for 5000 ppm $CO_2$ at 0.4 atm (dots), alongside the corresponding fit using HITRAN2020 database (green line). The vertical bars illustrate the isotopologues included in the fit, with their lengths proportional to the normalized strength of the transition lines, according to standard abundances as specified in the legend. The bottom plot shows the residuals, highlighting the differences between the experimental data and the database fit.

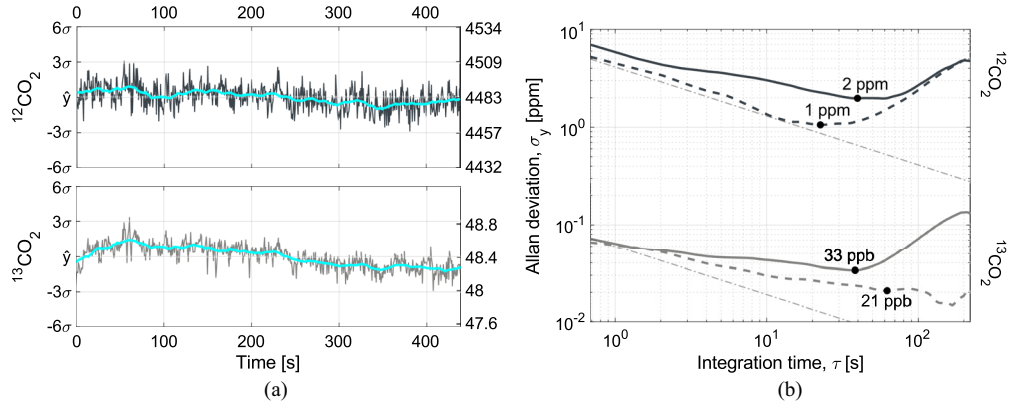


**Fig. 7.** (a) Concentration time series for $^{12}CO_2$ and $^{13}CO_2$ isotopes in a 5000 ppm $CO_2$ gas mixture. The black lines represent the raw data, while the 30 s moving average is displayed by light blue lines. The right vertical axes mark the concentration in ppm units, while the left vertical axes show the standard deviation $\sigma$ and are centered around the full measurement mean $\hat{y}$. (b) Corresponding Allan deviation plots (solid lines), as compared to zero-gas LoD obtained with pure $N_2$ (dashed lines).

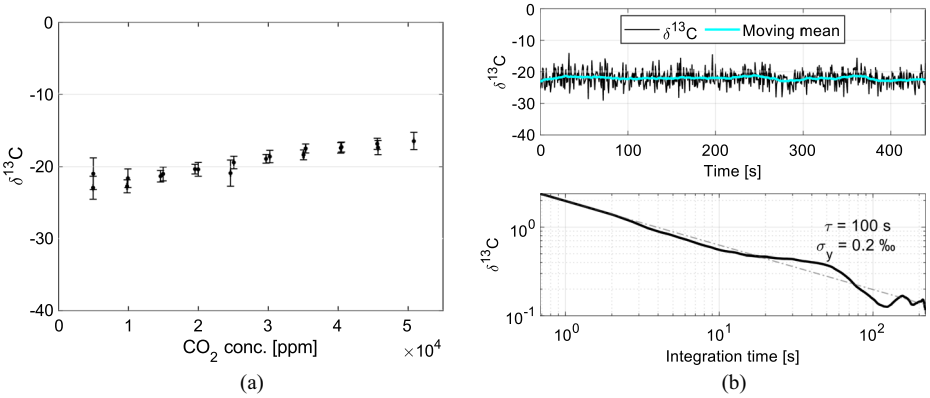


**Fig. 8.** (a) Isotope ratio $\delta^{13}C$ measured across the $CO_2$ concentration range of 5000–50000 ppm. The error bars represent the standard deviation indicating the precision for each concentration step. (b) The upper graph plots the time series of $\delta^{13}C$ at a constant $CO_2$ concentration of 5000 ppm (black line) together with a 30 s moving mean (cyan line). The bottom graph presents the corresponding Allan deviation plot, indicating a precision of 0.2‰ for 100 s of averaging.

the range from 5000 to 50000 ppm. As depicted in Fig. 8(a), the measured isotope ratio was not strictly stable with varying concentration, showing an increasing trend from −23‰ at 5000 ppm to −17‰ at 50000 ppm. This represents an error of ±3‰ across the full concentration range, which is not negligible but manageable through, e.g., more elaborate spectral processing or calibration. To evaluate the precision of the $\delta^{13}C$ measurements, we conducted Allan variance analysis of data measured at a fixed concentration of 5000 ppm over 450 s as depicted in Fig. 8(b). Such measurement resulted in an excellent precision of 0.2‰ after 100 s of averaging. Given the roughly constant error bar on $\delta^{13}C$ depicted in Fig. 8, we anticipate that this level of precision will be sustained across the entire 5000–50000 ppm concentration range. A decrease in precision can be naturally expected for very low $CO_2$ concentrations due to a gradual reduction in the signal-to-noise ratio.

## 5. DISCUSSION AND CONCLUSION

The demonstrated trace gas detection down to tens of ppb using an integrated waveguide, and the resulting ability to perform sensitive isotope ratio detection, represent two important milestones. Table 1 gives a comprehensive overview of the state of the art within on-chip gas spectroscopy, clearly indicating that the 20 ppb detection limit demonstrated here for $^{13}CO_2$ is an impressive improvement by five orders of magnitude compared to results achieved with other photonic on-chip $CO_2$ sensors. Compared to the state-of-the-art LoDs for other gases, this work still maintains a clear lead by one to two orders of magnitude.

The key to this success is the use of a waveguide with high external and low internal confinement factors of 102% and 4%, respectively, facilitating high light–analyte interaction and mitigating both propagation losses and spurious etalons. Additionally, the choice of a suitable driving and data analysis strategy including spectral fitting, similar to that employed in high-end free-space LAS setups, ensures low noise in our system. The apparent inferior performance for $^{12}CO_2$, exhibiting an order of magnitude higher LoD of 1 ppm compared to the LoD of 20 ppb for $^{13}CO_2$, is related to our selection of a weaker absorption line for $^{12}CO_2$ (linestrength of $2.75 \times 10^{-20}$ cm molecule$^{-1}$) relative to a stronger line for $^{13}CO_2$ (linestrength $2.68 \times 10^{-18}$ cm molecule$^{-1}$). As discussed earlier, this strategic choice was made to obtain comparable absorption of the two isotopes at their natural abundance and thus ensure optimal signal-to-noise ratio for the isotope ratio measurement. An LoD in the 10 ppb range can as well be achieved for the light $^{12}CO_2$ isotope through a shift of the laser wavelength to the main absorption band of $CO_2$ at, e.g., 4.283 μm.

**Table 1. Overview of Integrated Waveguide Sensors for Trace Gas Detection Operating on the Principle of IR Absorption**

| Waveguide Material | λ [μm] | $\Gamma_e$ [%] | α [dB/cm] | LoD [ppm] | Gas | TE/TM | Reference |
|---|---|---|---|---|---|---|---|
| SiN[a] | 4.345 | 102 | 3.43 | 0.02 | $CO_2$ | TM | This work |
| Si | 4.237 | 19.7 | 2.35 | 500 | $CO_2$ | TE | Lin *et al.* [29] |
| Si | 4.23 | 16 | 4.24 | 500 | $CO_2$ | TE | Ranacher *et al.* [30] |
| Si | 4.24 | 44 | 3 | 1000 | $CO_2$ | TE | Ottonello-Briano *et al.* [31] |
| Si on SiN[a] | 4.23 | 19.5 | - | 5000 | $CO_2$ | - | Ranacher *et al.* [32] |
| ChC on $MgF_2$ | 4.319 | 4.6 | 5.1 | 25000 (3000[b]) | $CO_2$ | TM | Pi *et al.* [33] |
| PMMA/ZIF-8 | 0.850 | - | - | 50000 | $CO_2$ | TE | Zheng *et al.* [34] |
| Si | 4.27 | 7.9 | - | 100000 | $CO_2$ | TE | Consani *et al.* [35] |
| Si | 3.2704 | 69 | 8.3 | 0.3 | $CH_4$ | TE | Yallew *et al.* [36] |
| Si/SiN | 1.65 | 25.4 | 2 | 100 | $CH_4$ | TM | Tombez *et al.* [37] |
| Si | 3.291 | 23.3 | 0.71 | 347 (85[b]) | $CH_4$ | TE | Zhao *et al.* [38] |
| $Ni_2O_5$ | 3.291 | 11.5 | 6.06 | 349[b] | $CH_4$ | TM | Bi *et al.* [39] |
| ChC on $MgF_2$ | 3.291 | 7.8 | 1.52 | 6800[b] | $CH_4$ | TM | Pi *et al.* [40] |
| Si[a] | 7.33 | 113 | 4.7 | 2.5 | $C_3H_6O$ | TE | Liu *et al.* [22] |
| $Ta_2O_5$[a] | 2.75 | 107 | 6.8 | 7 | $C_2H_2$ | TM | Vlk *et al.* [19] |
| Si[a] | 6.65 | 24.3 | 4.3 | 75 | $C_7H_8$ | TE | Liu *et al.* [41] |
| InGaAs[a] | 6.15 | 90.5 | 4.1 | 84 | $NH_3$ | TM | Yoo *et al.* [42] |

[a]Membrane waveguides.
[b]Wavelength modulation spectroscopy.

Achieving similar detection limits for other gases might be possible with slight adjustments to the waveguide's cross-sectional design. However, for wavelengths above 5 μm, the increased absorption of SiN could pose a challenge. This work has shown that material absorption can be effectively mitigated by using waveguide designs with low internal confinement factors. Yet, as absorption intensifies and the need to further decrease the internal confinement factor arises, the resultant extended field may conflict with the requirements for tightly folding long optical paths on a photonic chip. Therefore, in the far MIR range, replacing SiN with materials that offer better MIR transparency, such as chalcogenide glasses, would be beneficial.

Isotope-specific detection, enabling accurate and simultaneous quantification of two different $CO_2$ isotopes, allowed us to demonstrate the first-ever stable isotope ratio measurements conducted with a nanophotonic integrated waveguide. The sensitivity of 0.2‰ measured at a stable $CO_2$ concentration is truly exceptional, comparable to that of commercial high-end devices, while only an order of magnitude lower than the best measurements using LAS [43,44]. Yet, the drift of $\delta^{13}C$ registered with $CO_2$ concentration implies that the sensor calibration is necessary before deploying the sensor in real-world settings. This drift can be attributed to both the presence of residual etalons affecting the baseline definition, as well as line broadening changes upon varying gas composition. Further decrease of the pressure in the gas cell is one mitigation strategy, allowing for better separation between the respective isotopes and a more accurate baseline fit. However, drifts of similar or even higher magnitude of up to 15‰ in raw measurements are also reported [45] using high-end LAS instruments. This indicates that sub-‰ accuracy necessitates rigorous calibration and stable operating conditions (e.g., small range of sample concentrations) even when using the best available bulky instruments [46].

In summary, our suspended waveguide sensor merges the strengths of high-end commercial spectroscopic systems, offering sensitivity, selectivity, and isotope detection capability, while also being compact and lightweight. CMOS-compatible fabrication and rather straightforward integration of the sensor chip with laser and detection modules hold a promise that high-end chip-scale systems may soon emerge on the market, while being considerably more affordable and scalable than their bulky counterparts. The demonstrated isotope ratio precision is already adequate for various tasks in environmental monitoring or climate research. These applications can include on-site monitoring at the emission source or the creation of distributed sensor networks to provide large spatial coverage and data of unparalleled detail and density.

**Funding.** H2020 European Research Council (758973); Tromsø Forskningsstiftelse (17SGJJ); Norges Forskningsråd (295864); Ministerstvo Školství, Mládeže a Tělovýchovy (LasApp CZ.02.01.01/00/22 351 008/0004573).

**Acknowledgment.** We would like to acknowledge Henock D. Yallew, Jens Høvik, and Sveinung V. Olsen for their respective assistance with data analysis, cleanroom processing, and laser driving electronics.

**Disclosures.** The author declares no conflicts of interest.

**Data availability.** Data underlying the results presented in this paper are not publicly available at this time but may be obtained from the authors upon reasonable request.

**Supplemental document.** See Supplement 1 for supporting content.

## REFERENCES


1. K. B. Beć, J. Grabska, and C. W. Huck, "Chapter 1—Physical principles of infrared spectroscopy," in *Infrared Spectroscopy for Environmental Monitoring*, D. Cozzolino, ed., Vol. 98 of Comprehensive Analytical Chemistry (Elsevier, 2022), pp. 1–43.
2. J. Kostinek, A. Roiger, K. J. Davis, *et al.*, "Adaptation and performance assessment of a quantum and interband cascade laser spectrometer for simultaneous airborne in situ observation of $CH_4$, $C_2H_6$, $CO_2$, CO and $N_2O$," Atmos. Meas. Tech. **12**, 1767–1783 (2019).
3. R. J. Fleming, "An updated review about carbon dioxide and climate change," Environ. Earth Sci. **77**, 262 (2018).
4. H. Graven, R. F. Keeling, and J. Rogelj, "Changes to carbon isotopes in atmospheric $CO_2$ over the industrial era and into the future," Global Biogeochem. Cycles **34**, e2019GB006170 (2020).
5. H.-O. Pörtner and D. C. Roberts, "Climate change 2022: Impacts, adaptation and vulnerability," Tech. rep. (Intergovernmental Panel on Climate Change, 2022).
6. M. Denommé, J. E. Deakin, Y. E. Morbey, *et al.*, "Using breath $\delta^{13}C$ analysis to determine the effects of dietary carbohydrate and protein on glucose and leucine oxidation at rest in the yellow-rumped warbler (Setophaga coronata)," Comp. Biochem. Physiol. A **256**, 110936 (2021).
7. L. Bodner, S. Bouchebti, and E. Levin, "Allocation and metabolism of naturally occurring dietary amino acids in the oriental hornet," Insect Mol. Biol. **139**, 103675 (2021).
8. K. B. Tankersley, D. G. Conover, and D. L. Lentz, "Stable carbon isotope values ($\delta^{13}C$) of purslane (portulaca oleracea) and their archaeological significance," J. Archaeolog. Sci. **7**, 189–194 (2016).
9. B. J. Tipple, S. R. Meyers, and M. Pagani, "Carbon isotope ratio of cenozoic $CO_2$: A comparative evaluation of available geochemical proxies," Paleoceanography **25** (2010).
10. J. Reid, J. Shewchun, B. K. Garside, *et al.*, "High sensitivity pollution detection employing tunable diode lasers," Appl. Opt. **17**, 300–307 (1978).
11. J. Reid, M. El-Sherbiny, B. K. Garside, *et al.*, "Sensitivity limits of a tunable diode laser spectrometer, with application to the detection of $NO_2$ at the 100-ppt level," Appl. Opt. **19**, 3349–3353 (1980).
12. C. S. Goldenstein, R. M. Spearrin, J. B. Jeffries, *et al.*, "Infrared laser-absorption sensing for combustion gases," Prog. Energy Combust. Sci. **60**, 132–176 (2017).
13. J. Xia, C. Feng, F. Zhu, *et al.*, "A sensitive methane sensor of a ppt detection level using a mid-infrared interband cascade laser and a long-path multipass cell," Sens. Actuators B Chem. **334**, 129641 (2021).
14. I. Galli, S. Bartalini, R. Ballerini, *et al.*, "Spectroscopic detection of radiocarbon dioxide at parts-per-quadrillion sensitivity," Optica **3**, 385–388 (2016).
15. X. Lou, Y. Feng, S. Yang, *et al.*, "Ultra-wide-dynamic-range gas sensing by optical pathlength multiplexed absorption spectroscopy," Photonics Res. **9**, 193–201 (2021).
16. Z. Du and J. Li, "Spectroscopic gas sensing systems," in *Handbook of II-VI Semiconductor-Based Sensors and Radiation Detectors*, Vol. **3** of Sensors, Biosensors and Radiation Detectors (Springer, 2023), pp. 335–360.
17. W. Nam, C. Cho, B. Perdigones, *et al.*, "Development of a broadband cavity-enhanced absorption spectrometer for simultaneous measurements of ambient $NO_3$, $NO_2$, and $H_2O$," Atmos. Meas. Tech. **15**, 4473–4487 (2022).
18. G. Veldhuis, O. Parriaux, H. Hoekstra, *et al.*, "Sensitivity enhancement in evanescent optical waveguide sensors," J. Lightwave Technol. **18**, 677–682 (2000).
19. M. Vlk, A. Datta, S. Alberti, *et al.*, "Extraordinary evanescent field confinement waveguide sensor for mid-infrared trace gas spectroscopy," Light Sci. Appl. **10**, 677–682 (2021).
20. M. A. Webster, R. M. Pafchek, A. Mitchell, *et al.*, "Width dependence of inherent TM-mode lateral leakage loss in silicon-on-insulator ridge waveguides," IEEE Photonics Technol. Lett. **19**, 429–431 (2007).
21. D. M. Kita, J. Michon, S. G. Johnson, *et al.*, "Are slot and sub-wavelength grating waveguides better than strip waveguides for sensing?" Optica **5**, 1046–1054 (2018).
22. W. Liu, Y. Ma, X. Liu, *et al.*, "Larger-than-unity external optical field confinement enabled by metamaterial-assisted comb waveguide for ultrasensitive long-wave infrared gas spectroscopy," Nano Lett. **22**, 6112–6120 (2022).
23. J. Kischkat, S. Peters, B. Gruska, *et al.*, "Mid-infrared optical properties of thin films of aluminum oxide, titanium dioxide, silicon dioxide, aluminum nitride, and silicon nitride," Appl. Opt. **51**, 6789–6798 (2012).
24. K. Alexander, J. P. George, J. Verbist, *et al.*, "Nanophotonic Pockels modulators on a silicon nitride platform," Nat. Commun. **9**, 1–6 (2018).
25. J. T. Robinson, K. Preston, O. Painter, *et al.*, "First-principle derivation of gain in high-index-contrast waveguides," Opt. Express **16**, 16659–16669 (2008).
26. M. Vlk, A. Datta, S. Alberti, *et al.*, "Free-standing tantalum pentoxide waveguides for gas sensing in the mid-infrared," Opt. Mater. Express **11**, 3111–3124 (2021).
27. I. E. Gordon, L. S. Rothman, R. Hargreaves, *et al.*, "The hitran2020 molecular spectroscopic database," J. Quant. Spectrosc. Radiat. Transfer **277**, 107949 (2022).
28. H. Craig, "Isotopic standards for carbon and oxygen and correction factors for mass-spectrometric analysis of carbon dioxide," Geochim. Cosmochim. Acta **12**, 133–149 (1957).
29. P.-S. Lin, A. Quellmalz, P.-H. Huang, *et al.*, "Low-concentration detection of $CO_2$ using suspended silicon waveguides in the mid-IR," in *Conference on Lasers and Electro-Optics (CLEO)* (Optica Publishing Group, 2022), paper SF4O.1.
30. C. Ranacher, C. Consani, N. Vollert, *et al.*, "Characterization of evanescent field gas sensor structures based on silicon photonics," IEEE Photonics J. **10**, 2700614 (2018).
31. F. Ottonello-Briano, C. Errando-Herranz, H. Rödjegård, *et al.*, "Carbon dioxide absorption spectroscopy with a mid-infrared silicon photonic waveguide," Opt. Lett. **45**, 109–112 (2020).
32. C. Ranacher, C. Consani, A. Tortschanoff, *et al.*, "Mid-infrared absorption gas sensing using a silicon strip waveguide," Sens. Actuators A Phys. **277**, 117–123 (2018).
33. M. Pi, C. Zheng, H. Zhao, *et al.*, "Mid-infrared ChG-on-$MgF_2$ waveguide gas sensor based on wavelength modulation spectroscopy," Opt. Lett. **46**, 4797–4800 (2021).
34. L. Zheng, N. Keppler, H. Zhang, *et al.*, "Planar polymer optical waveguide with metal-organic framework coating for carbon dioxide sensing," Adv. Mater. Technol. **7**, 2200395 (2022).
35. C. Consani, C. Ranacher, A. Tortschanoff, *et al.*, "Mid-infrared photonic gas sensing using a silicon waveguide and an integrated emitter," Sens. Actuators B Chem. **274**, 60–65 (2018).
36. H. D. Yallew, M. Vlk, A. Datta, *et al.*, "Sub-PPM methane detection with mid-infrared slot waveguides," ACS Photonics **10**, 4282–4289 (2023).
37. L. Tombez, E. J. Zhang, J. S. Orcutt, *et al.*, "Methane absorption spectroscopy on a silicon photonic chip," Optica **4**, 1322–1325 (2017).
38. H. Zhao, C. Zheng, M. Pi, *et al.*, "On-chip mid-infrared silicon-on-insulator waveguide methane sensor using two measurement schemes at 3.291 μm," Front. Chem. **10**, 953684 (2022).
39. R. Bi, M. Pi, C. Zheng, *et al.*, "A niobium pentoxide waveguide sensor for on-chip mid-infrared absorption spectroscopic methane measurement," Sens. Actuators B Chem. **382**, 133567 (2023).
40. M. Pi, Y. Huang, H. Zhao, *et al.*, "Theoretical and experimental investigation of on-chip mid-infrared chalcogenide waveguide $CH_4$ sensor based on wavelength modulation spectroscopy," Sens. Actuators B Chem. **362**, 131782 (2022).
41. W. Liu, Y. Ma, Y. Chang, *et al.*, "Suspended silicon waveguide platform with subwavelength grating metamaterial cladding for long-wave infrared sensing applications," Nanophotonics **10**, 1861–1870 (2021).
42. K. M. Yoo, J. Midkiff, A. Rostamian, *et al.*, "InGaAs membrane waveguide: a promising platform for monolithic integrated mid-infrared optical gas sensor," ACS Sens. **5**, 861–869 (2020).
43. S. V. Kireev, A. A. Kondrashov, S. L. Shnyrev, *et al.*, "Methods of $^{14}CO_2$, $^{13}CO_2$, and $^{12}CO_2$ detection in gaseous media in real time," Laser Phys. **27**, 105701 (2017).
44. H. Zhang, M. Wen, Y. Li, *et al.*, "High- precision $^{13}CO_2/^{12}CO_2$ isotopic ratio measurement using tunable diode laser absorption spectroscopy at 4.3 μm for deep-sea natural gas hydrate exploration," Appl. Sci. **9**, 3444 (2019).
45. C. Rella, "White paper: Accurate stable carbon isotope ratio measurements in humid gas streams using the picarro $\delta^{13}CO_2$ G2101-i gas analyzer," Tech. rep. (Picarro Inc., 2012).
46. X.-F. Wen, Y. Meng, X.-Y. Zhang, *et al.*, "Evaluating calibration strategies for isotope ratio infrared spectroscopy for atmospheric $^{13}CO_2/^{12}CO_2$ measurement," Atmos. Meas. Tech. **6**, 1491–1501 (2013).